
01 Jan 2023

Synthesis, Densification, And Cation Inversion In High Entropy (Co,Cu,Mg,Ni,Zn)Al₂O₄ Spinel

Cole A. Corlett

Nina Obradovic

Jeremy Lee Watts

Missouri University of Science and Technology, jwatts@mst.edu

Eric W. Bohannon

Missouri University of Science and Technology, bohannon@mst.edu

et. al. For a complete list of authors, see https://scholarsmine.mst.edu/matsci_eng_facwork/3194

Follow this and additional works at: https://scholarsmine.mst.edu/matsci_eng_facwork

 Part of the [Chemistry Commons](#), and the [Materials Science and Engineering Commons](#)

Recommended Citation

C. A. Corlett et al., "Synthesis, Densification, And Cation Inversion In High Entropy (Co,Cu,Mg,Ni,Zn)Al₂O₄ Spinel," *Journal of Asian Ceramic Societies*, Taylor and Francis Group; Taylor and Francis, Jan 2023.

The definitive version is available at <https://doi.org/10.1080/21870764.2023.2227535>

This Article - Journal is brought to you for free and open access by Scholars' Mine. It has been accepted for inclusion in Materials Science and Engineering Faculty Research & Creative Works by an authorized administrator of Scholars' Mine. This work is protected by U. S. Copyright Law. Unauthorized use including reproduction for redistribution requires the permission of the copyright holder. For more information, please contact scholarsmine@mst.edu.

Synthesis, densification, and cation inversion in high entropy (Co,Cu,Mg,Ni,Zn)Al₂O₄ spinel

Cole A. Corlett, Nina Obradovic, Jeremy L. Watts, Eric W. Bohannan & William G. Fahrenholtz

To cite this article: Cole A. Corlett, Nina Obradovic, Jeremy L. Watts, Eric W. Bohannan & William G. Fahrenholtz (2023): Synthesis, densification, and cation inversion in high entropy (Co,Cu,Mg,Ni,Zn)Al₂O₄ spinel, Journal of Asian Ceramic Societies, DOI: [10.1080/21870764.2023.2227535](https://doi.org/10.1080/21870764.2023.2227535)

To link to this article: <https://doi.org/10.1080/21870764.2023.2227535>



© 2023 The Author(s). Published by Informa UK Limited, trading as Taylor & Francis Group on behalf of The Korean Ceramic Society and The Ceramic Society of Japan.



Published online: 29 Jun 2023.



[Submit your article to this journal](#)



Article views: 220




[View related articles](#)



[View Crossmark data](#)

Synthesis, densification, and cation inversion in high entropy (Co,Cu,Mg,Ni,Zn) Al₂O₄ spinel

Cole A. Corlett^a, Nina Obradovic ^b, Jeremy L. Watts^a, Eric W. Bohannon^a and William G. Fahrenholtz^a

^aMaterials research center, Missouri University of Science & Technology, Rolla, MO, USA; ^bMaterials research center, Institute of Technical Sciences of the Serbian Academy of Sciences and Arts, Belgrade, Serbia

ABSTRACT

The synthesis, densification behavior, and crystallographic site occupancy were investigated for four different spinel-based ceramics, including a high-entropy spinel (Co_{0.2}Cu_{0.2}Mg_{0.2}Ni_{0.2}Zn_{0.2})Al₂O₄. Each composition was reacted to form a single phase, but analysis of X-ray diffraction patterns revealed differences in cation site occupancy with the high-entropy spinel being nearly fully normal. Densification behavior was investigated and showed that fully dense ceramics could be produced by hot pressing at temperatures as low as 1375°C for all compositions. Vickers' hardness values were at least 10 GPa for all compositions. The cations present in the high-entropy spinel appear to have a stabilizing effect that led to nearly normal site occupancy compared to full cation inversion behavior of nickel aluminate spinel. This is the first report that compares cation site occupancy of a high-entropy spinel to conventional spinel ceramics.

ARTICLE HISTORY

Received 13 March 2023
Accepted 2 May 2023

KEYWORDS

Synthesis; sintering;
densification; spinel

1. Introduction

Magnesium aluminate, MgAl₂O₄, which is commonly referred to by its mineral name of spinel, is the only compound in the MgO-Al₂O₃ binary system. Interest in magnesium aluminate spinel ceramics is driven by properties such as high melting point (>2100°C), high hardness (~13 GPa), resistance to chemical attack, and the potential for optical transparency [1–3]. These exceptional properties are what allow magnesium aluminate spinel ceramics to be used in applications such as catalyst-supports, refractories, transparent armor, and radiation tolerant ceramics [4,5]. Several methods can be used to fabricate spinel-based ceramics, including direct solid-state reactions, wet chemical techniques, and mechanical activation techniques [6–14].



Spinel phases are also known in a variety of other systems. For example, cobalt aluminate spinel is a well-known pigment [15–17]. The color is impacted by the degree of cation site inversion with the most desired deep blue color formed when cobalt atoms are mainly located on the tetrahedral sites (i.e. the spinel in almost fully normal) [15]. Zinc aluminate spinel is a thermally stable catalyst support that has been reported to have zinc cations occupying a mixture of tetrahedral and octahedral sites [18]. Doping of spinels with different cations has been reported as a method for tuning photocatalytic properties [19].

The concept of entropy stabilization has been investigated in several classes of materials [20,21], ranging

from high-entropy alloys (HEAs) [22], high-entropy carbides (HECs) [23], borides (HEBs) [24], and oxides (HEOs) [25]. In 2004, Yeh [26] and Cantor [27] first proposed the idea of HEAs and multi-principal component alloys. Applying that concept to ceramics, Rost was the first to show entropic stabilization of five different cations in equimolar ratios in a single-phase oxide system, (Co_{0.2}Cu_{0.2}Mg_{0.2}Ni_{0.2}Zn_{0.2})O with a rock salt structure [28]. From the Rost study, it was concluded that the local bond lengths between the metals and oxygen varied around each cation, with a notable distortion around the Cu-O polyhedra.

The first HEO with the spinel structure, (Co,Cr,Fe,Mn,Ni)₃O₄ was synthesized in 2017 with the intent to confirm that these specific cations could be incorporated into a single spinel phase [29]. X-ray diffraction (XRD) analysis indicated that a pure, single-phase spinel material was synthesized from the constituent oxides. These results were further confirmed by energy-dispersive spectroscopy (EDS) and Raman spectroscopy. This material proved to be a good example for the formation of new HEO materials in that, different structures could form, depending on the oxygen partial pressure used during processing. This type of behavior, which is so different from HEAs, opens potential synthesis routes for HEO materials.

In the present study, the synthesis of a single-phase, high-entropy aluminate spinel (HES) based on the A-site cations Mg, Ni, Co, Cu, and Zn was studied.

CONTACT Nina Obradovic  nina.obradovic@itn.sanu.ac.rs  Institute of Technical Sciences of the Serbian Academy of Sciences and Arts, Knez Mihailova 35/IV, Belgrade 11000, Serbia

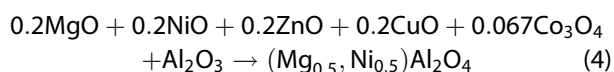
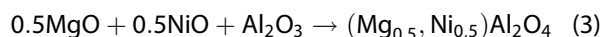
© 2023 The Author(s). Published by Informa UK Limited, trading as Taylor & Francis Group on behalf of The Korean Ceramic Society and The Ceramic Society of Japan. This is an Open Access article distributed under the terms of the Creative Commons Attribution-NonCommercial License (<http://creativecommons.org/licenses/by-nc/4.0/>), which permits unrestricted non-commercial use, distribution, and reproduction in any medium, provided the original work is properly cited. The terms on which this article has been published allow the posting of the Accepted Manuscript in a repository by the author(s) or with their consent.

This combination was chosen due to the similar atomic radii and the rock salt crystal structures from the parent oxides for MgO, NiO, and CoO and the previous studies showing that CuO and ZnO could be substituted into the rock salt structure in an HEO. The ability of the cations to be stable in the Me^{+2} oxidation state was also considered. The degree of cation inversion was characterized and compared to MgAl_2O_4 , $(\text{Mg}_{0.5}, \text{Ni}_{0.5})\text{Al}_2\text{O}_4$, and NiAl_2O_4 .

2. Materials and methods

2.1. Processing

Raw materials were batched to produce spinel powders with different compositions. Prior to batching, magnesium oxide powder ($\geq 99\%$, Sigma-Aldrich) was first calcined in air at 1000°C for 4 hours with a heating rate of $10^\circ\text{C}/\text{min}$ to decompose any carbonate, hydroxide, and/or hydroxycarbonate species to oxides. To produce the magnesium aluminate spinel, MgAl_2O_4 , (MAS), calcined magnesium oxide and $\alpha\text{-Al}_2\text{O}_3$ (A16-SG Almatix) were mixed in a one-to-one molar ratio according to Reaction 1. Likewise, nickel aluminate spinel, NiAl_2O_4 (NAS), was synthesized by mixing NiO (78.5 wt.% Ni, Alfa Aesar) and Al_2O_3 in a one-to-one molar ratio according to Reaction 2. A mixed, nickel-magnesium aluminate spinel, $(\text{Mg}_{0.5}, \text{Ni}_{0.5})\text{Al}_2\text{O}_4$, (NMAS) was produced by mixing equimolar amounts of calcined MgO and NiO with one molar equivalent of $\alpha\text{-Al}_2\text{O}_3$ according to Reaction 3. To produce the high-entropy spinel (HES), one molar equivalent of $\alpha\text{-Al}_2\text{O}_3$ was mixed with the appropriate amounts of calcined MgO, NiO, ZnO (99.9%, Alfa Aesar), CuO (97%, Alfa Aesar), and Co_3O_4 (99.7%, Alfa Aesar). The target composition was $(\text{Co}_{0.2}\text{Cu}_{0.2}\text{Mg}_{0.2}\text{Ni}_{0.2}\text{Zn}_{0.2})\text{Al}_2\text{O}_4$ based on the stoichiometry of Reaction 4. All mixing was accomplished by wet ball milling with ZrO_2 media in acetone for 24 h. The media to powder mass ratio was 3 to 1 in high-density polyethylene jars.



After the powders were mixed for 24 h, the slurries were dried by rotary evaporation (Rotovapor R-124; Buchi, Flawil, DEU). The dried powders were lightly ground to break large agglomerates and passed through an 80-mesh screen. After sieving, the powders were mechanically activated (MA) by high energy ball milling (Model No. 8000, Spex Industries, Inc.) with a cycle of 30 min on, 15 min off, and then the final 30

min for a total 60 min of active milling. The off time was added to minimize powder heating. Powders were loaded into an alumina mill jar with 5 mm alumina spherical media in increments of 12 g of powder with a media to powder mass ratio of 3:1. The milled powder mixtures were pushed through an 80-mesh screen. At this point, the milled powder mixtures were loaded into alumina crucibles and reacted at 1200°C for 2 h in a box furnace (Deltech, Colorado) in static air.

Dense ceramics were prepared by reactive hot pressing (RHP) in a 25.4 mm diameter graphite die lined with graphite paper (0.005"; Graftech International, Lakewood, USA) and coated with BN (SP-108; Materion, Milwaukee, USA). A tungsten metal sheet that was coated on both sides with BN was placed between the graphite paper and the powder compact to minimize interactions between the carbon dies and the specimens. Densification data were collected by measuring ram displacement using a linear variable differential transducer (LVDT) and analyzed using OriginLab graphical software to determine densification rates as a function of time during hot pressing. The hot press (HP; Model HP20-3060-20; Thermal Technology, Santa Rosa, USA) was heated under flowing argon at $25^\circ\text{C}/\text{min}$ to 1150°C and then $10^\circ\text{C}/\text{min}$ to 1200°C with a 2-h hold at 1200°C to allow the oxide precursors to react. After the 2-h hold, a uniaxial load of 32 MPa was applied, and the furnace heated at a rate of $25^\circ\text{C}/\text{min}$ to 50°C below the final hold temperature. It was at this point that data collection for densification began. The furnace was then heated at $10^\circ\text{C}/\text{min}$ to the final hold temperature of either 1375°C , 1450°C or 1550°C and was held for 30 min. The furnace was allowed to cool at $10^\circ\text{C}/\text{min}$ from the final hold temperature to 1200°C , at which point the load was removed and the furnace was allowed to cool at its natural rate. Specimens were surface ground to remove the tungsten sheet and any reaction layer. A modified Archimedes method was then used to measure the bulk density of each hot-pressed billet. The billets were then cross-sectioned and polished to a $0.25\ \mu\text{m}$ finish using successively finer diamond abrasives.

2.2. Characterization

Reacted powders were ground and passed through an 80-mesh screen prior to X-ray diffraction analysis (XRD; X'Pert Pro, PANalytical, Almelo, NLD) using Ni-filtered Cu-K α radiation. Phase analysis was performed by Rietveld refinement (RIQAS4, Materials Data Incorporated, Livermore, USA). Lattice parameters determined using Rietveld refinement of XRD data were used to calculate the theoretical density of the HES material assuming a cubic crystal structure and a space group number of $F\bar{4}3m$. Rietveld refinement was also used to estimate occupancies for the various

cation sites to determine the amount of inversion (i.e. occupancy of B sites such as Al by A site cations such as Mg). With this reference, a degree of inversion of 0.5 indicates a fully inverted spinel in which all of the A sites are occupied by Al cations. An initial refinement was performed for each material to get close to the site occupancy values for each material. Once that was done, refinements were performed by inputting specific occupancy values to determine where the site occupancy and fit error values converged. Precursor powders were analyzed for specific surface area (SSA) using the Brunauer–Emmett–Teller (BET) method (NOVA 2000e; Quantachrome Instruments, Boynton Beach, FL). Equivalent particle size was calculated by assuming that particles had a spherical shape. Calculated true densities (ρ) of each powder were also used in the calculation:

$$d = \frac{6}{SSA \cdot \rho} \quad (5)$$

Morphologies of both precursor and reacted powders were examined by scanning electron microscopy (SEM; Raith eLine, Raith GmbH, Islandia, New York). Powders were coated with a conductive Au/Pd layer before placing into SEM. Microhardness (H_v) was measured with a Vickers' diamond indenter (Duramin-5, Struers, Cleveland, OH), with 10 indents performed for each reported value. Phase analysis of polished sections of hot-pressed billets was performed using XRD. Grain size was measured using electron backscatter diffraction and image analysis (EBSD, Channel 5 software, Oxford Instruments) in SEM (Helios Nanolab 600, FEI)

by counting at least 1000 grains per composition. Grains were traced using GIMP photo editing software and grain sizes were analyzed for Feret's diameter using ImageJ.

3. Results and discussion

Heating to 1200°C produced crystalline MAS. Analysis of the XRD pattern (Figure 1) revealed that the specimen contained a single spinel phase and all peaks indexed to MAS with no other peaks present. The lattice parameter obtained for the MAS material was 8.08410 ± 0.00004 Å based on the Rietveld refinement fit (Table 1). The calculated true density using the nominal composition and the measured lattice parameter was 3.58 g/cm^3 , which agrees with previous reports [30]. Table 2 summarizes the XRD information with peak location and relative intensities. These peak locations and relative intensities matched most favorably with PDF# 74–1132 for MgAl_2O_4 .

Heating the NAS and NMAS materials to 1200°C produced crystalline materials with the spinel structure. Analysis of the XRD patterns (Figure 1) revealed that the specimens were each composed of a single spinel phase. The NAS pattern matched most closely with PDF# 78–1601. Each peak was indexed for NAS and NMAS, with peak positions and relative intensities presented in Table 1. The lattice parameters from the Rietveld refinements were 8.04839 ± 0.00005 Å for NAS and 8.06751 ± 0.00004 Å for NMAS. The theoretical densities calculated from the measured unit cell parameters and the nominal compositions were 4.50 g/cm^3

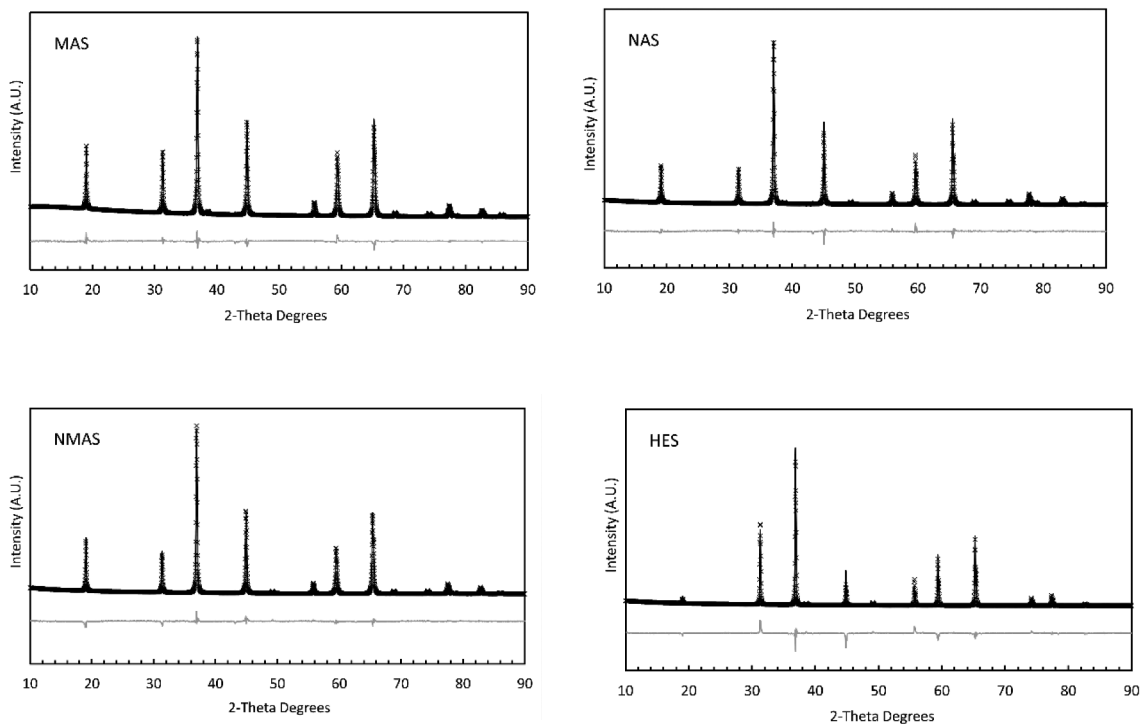


Figure 1. XRD patterns and Rietveld fits for (a) MAS, (b) NAS, (c) NMAS, and (d) HES.

Table 1. Indexed peaks of the four spinel materials.

Designation Plane	MAS		NAS		NMAS		HES	
	Peak Position (2 θ)	Relative Intensity (%)	Peak Position (2 θ)	Relative Intensity (%)	Peak Position (2 θ)	Relative Intensity (%)	Peak Position (2 θ)	Relative Intensity (%)
111	19.0	33.5	19.1	19.6	19.0	27.7	19.0	3.5
220	31.3	35.4	31.4	21.2	31.3	24.4	31.3	45.4
311	36.9	100	37.0	100	36.9	100	36.9	100.0
222	38.6	2.3	38.7	1.5	43.2	1.3	—	—
400	44.8	53.7	45.0	53.6	44.9	52.0	44.8	23.2
331	—	—	49.3	1.6	49.2	0.7	49.1	1.2
422	55.7	7.5	55.9	6.4	55.8	6.5	55.7	13.4
511	59.4	33.2	59.6	28.5	59.5	30.4	59.4	36.5
440	65.2	54.3	65.6	61.7	65.4	57.8	65.3	51.0
531	68.6	2.0	69.0	2.3	68.8	2.6	—	—
442	—	—	—	—	—	—	—	—
620	74.1	1.8	74.5	2.1	74.3	2.0	74.1	4.1
533	77.4	6.6	77.7	8.1	77.5	7.4	77.4	8.1
622	78.4	0.8	78.8	2.7	78.6	1.4	78.4	1.6
444	82.6	4.3	83.1	5.4	82.8	4.8	82.7	2.4
551	85.8	1.4	86.3	0.8	86.0	1.3	85.9	0.6

Table 2. Atomic positions, occupancies, lattice parameters and reliability factors for Rietveld refinement of MAS, NAS, NMAS and HES.

Atoms	Site	X	Y	Z	Occupancy
<i>MAS (Fd-3m), R_{wp} = 5.63%, R_p = 2.90%, R_{Bragg} = 2.81%</i>					
Mg1	8a	1/8	1/8	1/8	1.0
Al1	8a	1/8	1/8	1/8	0
Mg2	16d	1/2	1/2	1/2	0
Al2	16d	1/2	1/2	1/2	1.0
O	32e	0.256	0.256	0.256	1.0
<i>NAS (Fd-3m), R_{wp} = 2.90%, R_p = 1.61%, R_{Bragg} = 3.85%</i>					
Ni1	8a	1/8	1/8	1/8	.2
Al1	8a	1/8	1/8	1/8	.8
Ni2	16d	1/2	1/2	1/2	.4
Al2	16d	1/2	1/2	1/2	.6
O	32e	0.256	0.256	0.256	1.0
<i>NMAS (Fd-3m), R_{wp} = 3.19%, R_p = 1.78%, R_{Bragg} = 6.02%</i>					
Ni1/Mg1	8a	1/8	1/8	1/8	0
Al1	8a	1/8	1/8	1/8	1.0
Ni2/Mg2	16d	1/2	1/2	1/2	.5
Al2	16d	1/2	1/2	1/2	.5
O	32e	0.256	0.256	0.256	1.0
<i>HES (Fd-3m), R_{wp} = 4.27%, R_p = 1.60%, R_{Bragg} = 7.56%</i>					
Ni1/Mg1/Zn1/Cu1/Co1	8a	1/8	1/8	1/8	1.0
Al1	8a	1/8	1/8	1/8	0
Ni2/Mg2/Zn2/Cu2/Co2	16d	1/2	1/2	1/2	0
Al2	16d	1/2	1/2	1/2	1.0
O	32e	0.256	0.256	0.256	1.0

for NAS and 4.03 g/cm³ for NMAS. The calculated value for NAS agrees with the accepted density of 4.51 g/cm³ and the density for NMAS is consistent with the composition since lighter Mg atoms replace half of the Ni atoms in the structure.

Heating to 1200°C was sufficient to produce a nominally phase pure high-entropy spinel. Analysis of the XRD pattern (Figure 1) shows that the specimen contained a single phase that could be indexed to the spinel structure with no additional peaks present. The calculated lattice parameter was 8.08307 ± 0.00004 Å

with an estimated true density of 4.33 g/cm³. The positions of the peaks present in the HES material matched well pattern predicted for the modified spinel structure containing Mg, Ni, Zn, Cu, and Co.

Rietveld refinement was used to estimate the site occupancies of the cations in the spinel structure for the various powders. Table 2 lists the atomic positions, initial site occupancy assumptions, and reliability factors for the Rietveld refinements while Table 3 summarizes the site occupancies from the best fits along with predicted lattice parameters and true densities for

Table 3. Summary of Rietveld refinement results of the spinel powders.

Designation	Degree of Inversion	a-axis _{measured} (Å)	Theoretical Density (g/cm ³)
MAS	0.0	8.084 ± 0.00004	3.58
NAS	0.4	8.048 ± 0.00005	4.50
NMAS	0.5	8.068 ± 0.00004	4.03
HES	0.0	8.083 ± 0.00004	4.33

each composition. Rietveld refinement of XRD data was unable to provide unambiguous site occupancy for MAS because the X-ray scattering cross sections of Mg and Al are similar (i.e. 12 for Mg and 13 for Al). The degree of site inversion for MAS typically ranges from 0.1 to 0.5, depending on processing routes [31,32]. For example, our previous study found that mixed MgAl_2O_4 powders had inversion parameters that decreased from 0.19 for powder heated to 1200°C to 0.13 after heating to 1500°C [33]. In contrast, NAS is an inverse spinel that typically has Al atoms occupying all of the tetrahedral lattice sites and Ni atoms occupying half of the octahedral lattice sites. The other half of the octahedral sites are filled by Al atoms. Fit error values of about 5% or less were found for simulations that assumed full inversion for NAS and NMAS. Based on the Rietveld refinement and the varying peak intensities, NMAS and NAS appear to have a high degree of inversion (i.e. they are nearly fully inverted with values approaching 0.5 that indicate that half of the B sites are occupied by A cations). In contrast, HES appears to have a very low degree of inversion. Apparently, the presence of multiple divalent cations (Mg, Ni, Zn, Cu, and Co) promotes the formation of a normal spinel in which the divalent cations occupy nearly all of the A sites in the lattice resulting in a very low degree of cation inversion.

Mechanical activation reduced the starting particle sizes of the powders and homogenized the constituents. Table 4 summarizes the specific surface area (SSA) for milled and unmilled precursor powders along with equivalent particle sizes calculated from SSA. The SSA of each of the powders increased significantly after milling. Each starting (i.e. mixed) powder had a surface area of approximately 6 m²/g and the surface areas increased for the milled powders to the range of 7.0–7.5 m²/g, which is an increase in SSA of approximately 20%. Examining powder morphology showed that the most noticeable difference between unmilled and milled powders was the absence of micron-sized particles in the milled powders (Figure 2). The circle in Figure 2(a) highlights a large particle that was ~1 μm in diameter in the unmilled powder. Similar large particles were commonly observed in mixed powders, but none were found in milled powders. Other than the presence of a small fraction of large particles, the starting powders appeared to be sub-micron in size

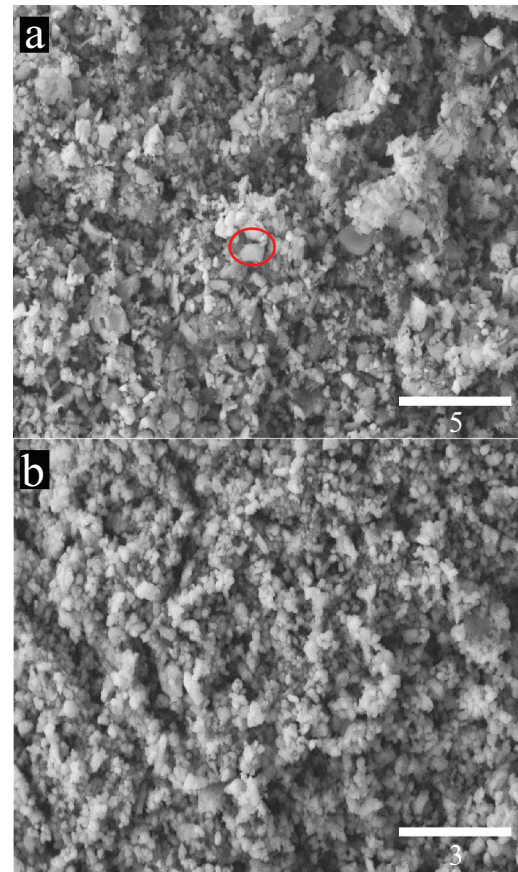


Figure 2. SEM micrographs of (a) as-mixed (b) milled HES powders after annealing at 1200°C for 2 hours. The red circle highlights a larger particle present in the mixed material that is largely missing from the milled powder.

with an irregular polygon shape and did not change appreciably after milling. These observations match with the measured SSA as seen in Table 4. Hence, mechanical activation led to reduction in the number of large particles, which presumably increased the reactivity of the material that enabled formation of single-phase ceramics of the desired compositions.

Densification curves for the milled HES at three different temperatures are shown in Figure 3. All specimens reached >98% relative density as summarized in Table 5. The specimen hot pressed at 1375°C reached full density during the isothermal hold, but the other two reached full density well before the final hold temperature was reached. It should be noted that the specimen with the largest initial densification rate was the specimen sintered at 1375°C, which was a rate of

Table 4. Specific surface area and theoretical particle size of unreacted prepared powders.

Designation	Type	SSA (m ² /g)	SSA % Increase	Theoretical Particle Size (μm)
MAS	Unmilled	5.8	22	0.29
	Milled	7.0		0.24
NAS	Unmilled	5.6	52	0.24
	Milled	8.5		0.16
NMAS	Unmilled	5.9	20	0.25
	Milled	7.1		0.21
HES	Unmilled	6.0	23	0.23
	Milled	7.4		0.19

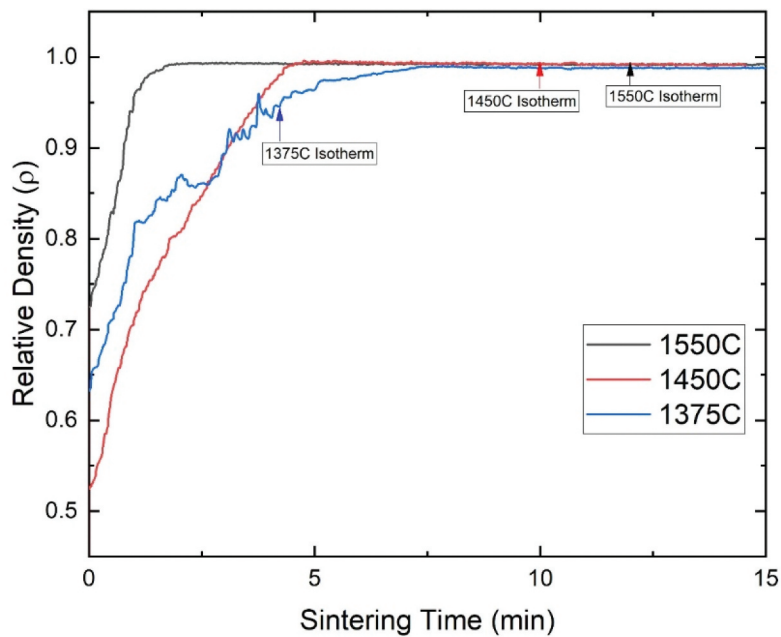


Figure 3. Relative density as a function of sintering time for HES powders. The sintering time begins when pressure was applied to the powder compacts. The arrows denote when the compacts reached the final sintering temperature.

Table 5. Densification rates and final densities for the three hot-pressed HES specimens.

Hold Temperature (°C)	Initial Densification Rate (min^{-1})	Bulk Density (g/cm^3)	Relative Density (%)
1375	6.2	4.27 ± 0.01	98.6 ± 0.2
1450	3.8	4.25 ± 0.01	98.0 ± 0.2
1550	4.3	4.29 ± 0.01	99.0 ± 0.1

6.2 min^{-1} as determined from the slope of the densification curve in Figure 3. The other two specimens had initial densification rates of 2.8 min^{-1} for sintering at 1450°C and 4.3 min^{-1} for sintering at 1550°C . Despite these differences in initial densification rates, all specimens reached relative densities of more than 98% based on the bulk density determined by Archimedes method and the theoretical density calculated from

the measured lattice parameters and nominal compositions.

Microhardness was measured for the hot-pressed materials at loads of 4.90 N and 9.81 N. These results along with the measured grain sizes are reported in Table 6 and a representative indentation can be seen in Figure 4. The indents were valid with no spalling noted and radial-median cracks appearing from the

Table 6. Vickers hardness values and grain sizes for hot pressed HES samples.

Sintering Temperature (°C)	Load (N)	H_v (GPa)	Grain Size (μm)
1375	4.90	14.1 ± 0.5	5.4
	9.81	14.0 ± 0.5	
1450	4.90	14.8 ± 0.4	5.4
	9.81	13.3 ± 0.6	
1550	4.90	14.4 ± 0.4	7.6
	9.81	13.2 ± 0.2	

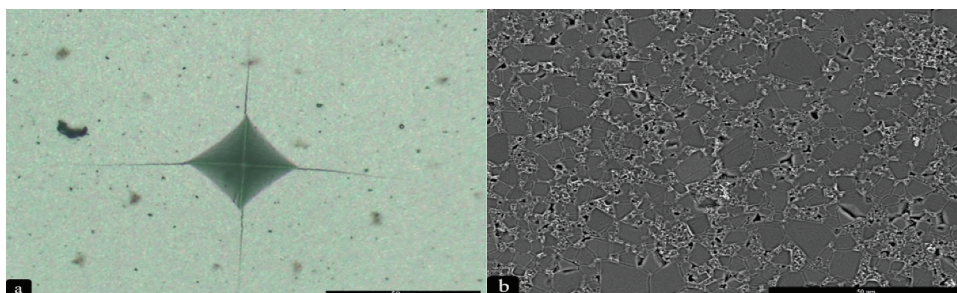


Figure 4. a) Representative vickers indent of the hot-pressed HES material sintered at 1375°C , b) representative image of grain size boundaries in HES material.

corners. The sample sintered at 1375°C had nearly the same hardness at each load with H_v of 14.1 ± 0.5 GPa at 4.90 N and 14.0 ± 0.5 GPa at 9.81 N. The sample prepared at 1450°C had a hardness of 14.8 ± 0.4 GPa at 4.90 N and 13.3 ± 0.6 GPa at 9.8 N. The sample sintered at 1550°C had similar hardness values calculated for each load with H_v of 14.4 ± 0.4 GPa at 4.90 N and 13.2 ± 0.2 GPa 9.81 N. The values reported in the present study are comparable to previous reports such as Haney [34], who reported hardness values of 14.1 GPa for transparent MAS with a grain size of $\sim 250 \mu\text{m}$.

4. Conclusions

The densification, site occupancy, and hardness of a high-entropy spinel were reported. A spinel with the nominal composition of $(\text{Co}_{0.2}\text{Cu}_{0.2}\text{Mg}_{0.2}\text{Ni}_{0.2}\text{Zn}_{0.2})\text{Al}_2\text{O}_4$ and three other spinel materials were synthesized. The NAS and NMAS materials were nearly fully inverse spinels whereas the HES had a low degree of inversion. Mechanical activation increased the SSA of the powders by about 25% due to elimination of large particles from the mixture. Vickers' hardness values of the HES were all around 14 GPa, which is higher than hardness values reported for MAS at the same load. The research presented here demonstrates a robust method for the synthesis and densification of spinel and high-entropy oxide materials. In addition, the effect of multiple cations appears to drive the system toward the formation of normal spinel in which the divalent cations are on the A sites in the spinel lattice.

Acknowledgments

This research was partially funded by the Enabling Materials for Extreme Environments signature area at Missouri S&T. The authors would like to thank the Advanced Materials Characterization Lab at Missouri S&T for use of the characterization equipment.

Disclosure statement

No potential conflict of interest was reported by the author(s).

ORCID

Nina Obradovic  <http://orcid.org/0000-0002-7993-293X>

References

- [1] Goldstein A, Goldenberg A, Yeshurun Y, et al. Transparent MgAl_2O_4 spinel from a powder prepared by flame spray pyrolysis. *J Am Ceram Soc.* 2008;91(12):4141–4144. doi: 10.1111/j.1551-2916.2008.02788.x
- [2] Ianoş R, Lazău I, Păcurariu C, et al. Solution combustion synthesis of MgAl_2O_4 using fuel mixtures. *Mater Res Bull.* 2008;43(12):3408–3415. doi: 10.1016/j.materresbull.2008.02.003
- [3] Esposito L, Piancastelli A, Martelli S. Production and characterization of transparent MgAl_2O_4 prepared by hot pressing. *J Eur Ceram Soc.* 2013;33(4):737–747. doi: 10.1016/j.jeurceramsoc.2012.10.013
- [4] Ganesh I. A review on magnesium aluminate (MgAl_2O_4) spinel: synthesis, processing and applications. *Inter Mat Rev.* 2013;58(2):63–112. doi: 10.1179/1743280412Y.0000000001
- [5] Guo J, Lou H, Zhao H, et al. Dry reforming of methane over nickel catalysts supported on magnesium aluminate spinels. *Appl Cat A General.* 2004;273(1–2):75–82. doi: 10.1016/j.apcata.2004.06.014
- [6] Devanathan R, Yu N, Sickafus KE, et al. Elastic instability in ion-beam-irradiated magnesium aluminate spinel. *Phil Mag B.* 2006;75(6):793–801. doi: 10.1080/13642819708205707
- [7] Obradovic N, Fahrenholtz W, Filipovic S, et al. Characterization of MgAl_2O_4 sintered ceramics. *Sc Sinter.* 2019;51(4):363–376. doi: 10.2298/SOS1904363O
- [8] Obradović N, Fahrenholtz WG, Filipović S, et al. The effect of mechanical activation on synthesis and properties of MgAl_2O_4 ceramics. *Ceram Int.* 2019;45(9):12015–12021. doi: 10.1016/j.ceramint.2019.03.095
- [9] Reimanis I, Kleebe HJ. A review on the sintering and microstructure development of transparent spinel (MgAl_2O_4). *J Am Ceram Soc.* 2009;92(7):1472–1480. doi: 10.1111/j.1551-2916.2009.03108.x
- [10] Sokol M, Halabi M, Kalabukhov S, et al. Nanostructured MgAl_2O_4 spinel consolidated by high pressure spark plasma sintering (HPSPS). *J Eur Ceram Soc.* 2017;37(2):755–762. doi: 10.1016/j.jeurceramsoc.2016.09.037
- [11] Ye G, Troczynski T. Mechanical activation of heterogeneous sol-gel precursors for synthesis of MgAl_2O_4 spinel. *J Am Ceram Soc.* 2005;88(10):2970–2974. doi: 10.1111/j.1551-2916.2005.00533.x
- [12] Dwibedi D, Avdeev M, Barpanda P, et al. Role of fuel on cation disorder in Magnesium Aluminate (MgAl_2O_4) spinel prepared by combustion synthesis. *J Am Ceram Soc.* 2015;98(9):2908–2913. doi: 10.1111/jace.13705
- [13] Bratton RJ. Co-precipitates yielding MgAl_2O_4 spinel powders. *Am Ceram Soc Bull.* 1969;48(8):759–762.
- [14] Li JG, Ikegami T, Lee JH, et al. A wet-chemical process yielding reactive magnesium aluminate spinel (MgAl_2O_4) powder. *Ceram Int.* 2001;27(4):481–489. doi: 10.1016/S0272-8842(00)00107-3
- [15] Yaemphutchong S, Wattanathana W, Chansaenpak K, et al. Structural investigation and optical properties of cobalt aluminate pigments derived from thermal decomposition of mixed-metal nitrate co-crystals. *Ceram Int.* 2022;48(13):18490–18501. doi: 10.1016/j.ceramint.2022.03.118
- [16] Tatarchuk T, Shyichuk A, Lamkiewicz J, et al. Inversion degree, morphology and colorimetric parameters of cobalt aluminate nanopigments depending on reductant type in solution combustion synthesis. *Ceram Int.* 2020;46(10):14674–14685. doi: 10.1016/j.ceramint.2020.02.269
- [17] Han M, Wang Z, Xu Y, et al. Physical properties of MgAl_2O_4 , CoAl_2O_4 , NiAl_2O_4 , CuAl_2O_4 , and ZnAl_2O_4 spinels synthesized by a solution combustion method.

- Mater Chem Phys. 2018;215:251–258. doi: [10.1016/j.matchemphys.2018.05.029](https://doi.org/10.1016/j.matchemphys.2018.05.029)
- [18] Yang C, Zhu W, Sen S, et al. Site inversion induces thermodynamic stability against coarsening in Zinc Aluminate spinel. *J Phys Chem C*. 2019;123(14):8818–8826. doi: [10.1021/acs.jpcc.8b11378](https://doi.org/10.1021/acs.jpcc.8b11378)
- [19] Tangcharoen T, Klysubun W, T-Thienprasert J, et al. Cation exchange in Ni–Cu–Zn aluminate spinels revealed by EXAFS. *J Solid State Chem*. 2020;292:121695. doi: [10.1016/j.jssc.2020.121695](https://doi.org/10.1016/j.jssc.2020.121695)
- [20] Oses C, Toher C, Curtarolo S. High entropy ceramics. *Nat Rev Mat*. 2020;5(4):295–309. doi: [10.1038/s41578-019-0170-8](https://doi.org/10.1038/s41578-019-0170-8)
- [21] Akrami S, Edalati P, Fuji M, et al. High entropy ceramics: review of principles, production, and applications. *Mat Sci And Eng R Rep*. 2021;146:100644. doi: [10.1016/j.mser.2021.100644](https://doi.org/10.1016/j.mser.2021.100644)
- [22] Tsai MH, Yeh JW. High-entropy alloys: a critical review. *Mat Res Lett*. 2014;2(3):107–123. doi: [10.1080/21663831.2014.912690](https://doi.org/10.1080/21663831.2014.912690)
- [23] Zhou J, Zhang J, Zhang F, et al. High-entropy carbide: a novel class of multicomponent ceramics. *Ceram Int*. 2018;44(17):22014–22018. doi: [10.1016/j.ceramint.2018.08.100](https://doi.org/10.1016/j.ceramint.2018.08.100)
- [24] Gild J, Zhang Y, Harrington T, et al. High-entropy metal diborides: a new class of high-entropy materials and a new type of ultrahigh temperature ceramics. *Sci Rep*. 2016;6(1):37946. doi: [10.1038/srep37946](https://doi.org/10.1038/srep37946)
- [25] Rost CM, Rak Z, Brenner DW, et al. Local structure of the $Mg_xNi_xCo_xCu_xZn_xO(x=0.2)$ entropy-stabilized oxide: an EXAFS study. *J Am Ceram Soc*. 2017;100(6):2732–2738. doi: [10.1111/jace.14756](https://doi.org/10.1111/jace.14756)
- [26] Yeh JW, Chen SK, Lin SJ, et al. Nanostructured high-entropy alloys with multiple principal elements: novel alloy design concepts and outcomes. *Adv Eng Mat*. 2004;6(5):299–303. doi: [10.1002/adem.200300567](https://doi.org/10.1002/adem.200300567)
- [27] Cantor B, Chang ITH, Knight P, et al. Microstructural development in equiatomic multicomponent alloys. *Mat Sci And Eng A*. 2004;375–377:213–218. doi: [10.1016/j.msea.2003.10.257](https://doi.org/10.1016/j.msea.2003.10.257)
- [28] Rost CM, Sachet E, Borman T, et al. Entropy-stabilized oxides. *Nat Commun*. 2015;6(1):1–8. doi: [10.1038/ncomms9485](https://doi.org/10.1038/ncomms9485)
- [29] Dąbrowa J, Stygar M, Mięka A, et al. Synthesis and microstructure of the $(Co,Cr,Fe,Mn,Ni)_3O_4$ high entropy oxide characterized by spinel structure. *Mat Lett*. 2018;216:32–36. doi: [10.1016/j.matlet.2017.12.148](https://doi.org/10.1016/j.matlet.2017.12.148)
- [30] Grzesik Z, Smoła G, Miszczak M, et al. Defect structure and transport properties of $(Co,Cr,Fe,Mn,Ni)_3O_4$ spinel-structured high entropy oxide. *J Eur Ceram Soc*. 2020;40(3):835–839. doi: [10.1016/j.jeurceramsoc.2019.10.026](https://doi.org/10.1016/j.jeurceramsoc.2019.10.026)
- [31] Sickafus KE, Wills JM, Grimes NW. Structure of spinel. *J Am Ceram Soc*. 1999;82(12):3279–3292. doi: [10.1111/j.1151-2916.1999.tb02241.x](https://doi.org/10.1111/j.1151-2916.1999.tb02241.x)
- [32] O'Quinn EC, Shamblin J, Perlov B, et al. Inversion in $Mg_{1-x}Ni_xAl_2O_4$ spinel: new insight into local structure. *J Am Chem Soc*. 2017;139(30):10395–10402. doi: [10.1021/jacs.7b04370](https://doi.org/10.1021/jacs.7b04370)
- [33] Corlett CA, Frontzek MD, Obradovic N, et al. Mechanical activation and cation site disorder in $MgAl_2O_4$. *Mat*. 2022;15(18):6422. doi: [10.3390/ma15186422](https://doi.org/10.3390/ma15186422)
- [34] Haney EJ, Subhash G, Zok F. Rate sensitive indentation response of a coarse-grained magnesium aluminate spinel. *J Am Ceram Soc*. 2011;94(11):3960–3966. doi: [10.1111/j.1551-2916.2011.04756.x](https://doi.org/10.1111/j.1551-2916.2011.04756.x)